







**Electronic and magnetic properties of intermetallic kagome magnets  $RV_6Sn_6$  ( $R = Tb - Tm$ )**Xiaoxiao Zhang <sup>1,2</sup>, Ziyi Liu,<sup>1</sup> Qi Cui,<sup>1</sup> Qi Guo,<sup>1,2</sup> Ningning Wang <sup>1,2</sup>, Lifen Shi,<sup>1,2</sup> Hua Zhang,<sup>1</sup> Weihua Wang,<sup>1,2,3</sup> Xiaoli Dong <sup>1,2,3</sup>, Jianping Sun <sup>1,2</sup>, Zhiling Dun <sup>1,2,\*</sup> and Jinguang Cheng <sup>1,2,†</sup><sup>1</sup>Beijing National Laboratory for Condensed Matter Physics and Institute of Physics, Chinese Academy of Sciences, Beijing 100190, China<sup>2</sup>School of Physical Sciences, University of Chinese Academy of Sciences, Beijing 100190, China<sup>3</sup>Songshan Lake Materials Laboratory, Dongguan, Guangdong 523808, China

(Received 13 June 2022; accepted 27 September 2022; published 10 October 2022)

We present a systematic study of the structure, electronic, and magnetic properties of a new branch of intermetallic compounds,  $RV_6Sn_6$  ( $R = Tb - Tm$ ) by using x-ray diffraction, magnetic susceptibility, magnetization, electrical transport, and heat-capacity measurements. These compounds feature a combination of a nonmagnetic vanadium kagome sublattice and a magnetic rare-earth triangular sublattice that supports various spin anisotropies based on different  $R$  ions. We find magnetic orders for the  $R = Tb$ ,  $Dy$ , and  $Ho$  compounds at 4.4, 3, and 2.5 K, respectively, while no ordering is detected down to 0.4 K for the  $R = Er$  and  $Tm$  compounds with easy-plane anisotropies. Electronically, we found no superconductivity or charge ordering transition down to 0.4 K for any member of this family, while all compounds exhibit multiband transport properties.

DOI: [10.1103/PhysRevMaterials.6.105001](https://doi.org/10.1103/PhysRevMaterials.6.105001)**I. INTRODUCTION**

Kagome metals have been at the forefront of condensed matter physics due to the quantum-level interplay between geometry, topology, and correlation [1–8]. On one hand, local moments on a lattice formed by corner-shared triangles induce strong frustration which serves as an important ingredient in realizing quantum spin liquids [1,9,10]. On the other hand, the electronic band structure of kagome lattice usually gives rise to flat bands, inflection points, and Dirac cones that promote nontrivial topology [3,6,7,11–16]. The combination of these effects usually gives rise to exotic states with possible capabilities of magnetic field and high-pressure engineering.

As an example, a recently discovered family of kagome metals,  $AV_3Sb_5$  ( $A = K, Rb, Cs$ ), has attracted tremendous research interest as a novel platform to study the interplay between nontrivial band topology, superconductivity, and charge density-wave (CDW) order [17–23]. The most prominent feature of this structure is the presence of a kagome net of vanadium atoms that are coordinated by  $Sb$  atoms, giving rise to  $Z_2$  topological states with Dirac nodal points near the Fermi level [17,19,20]. Meanwhile, superconductivity was discovered at ambient pressure below 0.93, 0.92, and 2.5 K for  $A = K, Rb$ , and  $Cs$  compounds, respectively [18–20,22,23], which was found to compete with an unusual charge order at high temperature [21,24–26]. This example shows the urgent need to explore the unusual superconductivity of other vanadium-based kagome intermetallics.

Another large family of kagome metal is  $RM_6X_6$  which crystallize in the  $MgFe_6Ge_6$  structural prototype. The  $R$  site hosts a variety of rare-earth ions ( $Y, Gd - Lu$ ),  $M$  is  $3d$

transition metal elements (e.g.,  $Co, Cr, Mn, V, Ni...$ ), and the  $X$  site is generally restricted to the group-IV elements ( $Si, Ge, Sn$ ). In these compounds,  $M$  atoms form a kagome lattice and  $R$  atoms form a triangular lattice; the two sublattices are stacked along the  $c$  axis in the ABA sequence to form a hexagonal structure [Figs. 1(a) and 1(b)]. Among them,  $RMn_6Sn_6$  has recently received the most attention due to the coexistence of topological band structure and magnetic order [16,27,28]. With the  $Mn$ -sublattice ordering at room temperature, the spin-orbit coupling and the ferromagnetic moment outside the  $ab$  plane open an energy gap near the Fermi surface, giving rise to Chern gapped Dirac fermion properties [16,27]. An important feature of the system is that both the  $Mn$  and  $R$  sublattices possess localized magnetic moments which are strongly coupled with each other. Recent study has demonstrated a close relationship between rare-earth magnetism and topological electron structure, indicating that the rare-earth elements can effectively engineer the Chern quantum phase in these materials [27,28]. This is partially reflected in the distinct  $Mn$ - $R$  spin orientations with different  $R$  sublattice. The magnetic anisotropy varies from easy plane for  $R = Gd$ , easy axis for  $R = Tb$ , to a conical magnetic structure for  $R = Dy$  and  $Ho$  [29–31]. When  $R = Er, Tm$ , the  $Mn$  and rare-earth sublattices order independently in an antiferromagnetic manner because the strength of the magnetic coupling is weak [30,31]. In this sense, further understanding of the electronic and magnetic properties in  $RMn_6Sn_6$  requires an in-depth understanding of the  $R$ -sublattice magnetism.

In this work, we explore a new family of V-based kagome metals  $RV_6Sn_6$ , and systematically study the structural, electronic, and magnetic properties for  $R = Gd - Tm$  compounds. These compounds are isostructural to its  $RMn_6Sn_6$  cousin and possess a similar nonmagnetic vanadium kagome sublattice as  $AV_3Sb_5$ . Four members of this family have been investigated very recently. Specifically, studies have

\*dun@iphy.ac.cn

†jgcheng@iphy.ac.cn

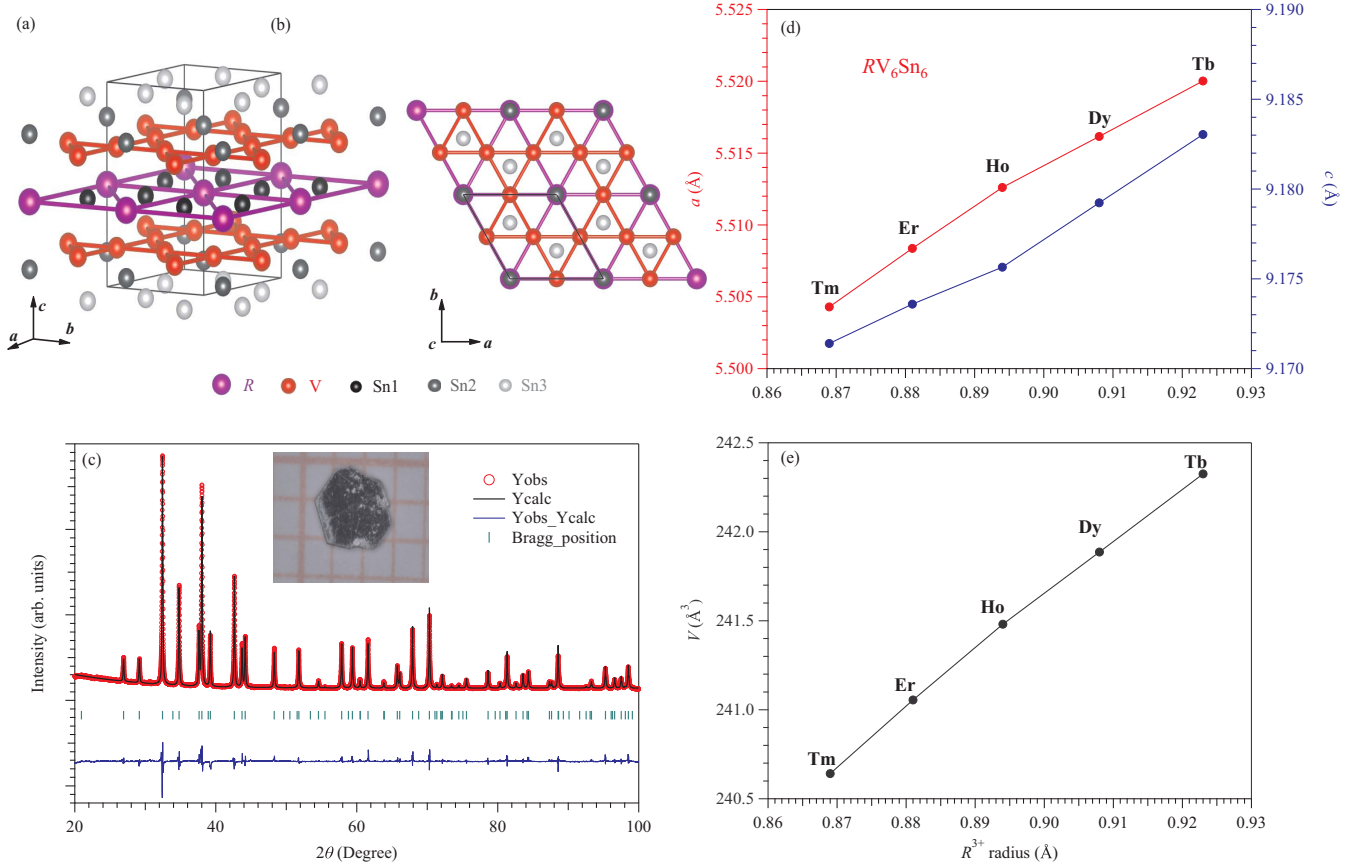


FIG. 1. (a) Crystal structure of  $RV_6Sn_6$  showing alternating kagome and triangular layers. (b) Top view of crystal structure from the  $c$  axis. (c) Observed (red circle), calculated (black line), and difference (blue line) profiles of the powder XRD patterns of  $DyV_6Sn_6$  from Rietveld refinements. Inset of (c) shows the photo of a millimeter-size  $DyV_6Sn_6$  single crystal. Ionic radii dependence of (d) cell parameters  $a$  and  $c$ , and (e) the unit cell volume.

identified two-dimensional kagome surface states in  $HoV_6Sn_6$  and  $GdV_6Sn_6$  [32,33], quantum oscillation in  $YV_6Sn_6$  [33], and CDW transition at 92 K in  $ScV_6Sn_6$  [34]. Compared to  $RMn_6Sn_6$ , the absence of Mn-Mn and Mn-R couplings enables us to study the intrinsic rare-earth magnetism on a frustrated triangular lattice. By combining the experimental probes of x-ray diffraction (XRD), DC magnetic susceptibility [ $\chi(T)$ ] and isothermal magnetization [ $M(H)$ ], and heat capacity [ $C_p(T)$ ], as well as transport measurements including resistivity [ $\rho(T)$ ], magnetoresistance [ $MR(H)$ ], and Hall resistivity [ $\rho_{xy}(H)$ ], we show that (i) there is no superconductivity or charge ordering transition down to 0.4 K for any member of this family; (ii) all compounds exhibit multiband transport properties that originate from the electronic bands of the vanadium kagome sublattice; (iii) with either strong ( $R = Tb$ ) or weak ( $R = Dy, Ho$ ) easy-axis anisotropies, the system orders at 4.4, 3, and 2.5 K, respectively; and (iv) with easy-plane anisotropy, no magnetic ordering is detected down to 0.4 K for the  $R = Er$  and  $Tm$  compounds.

## II. EXPERIMENTAL DETAILS

Single crystals of  $RV_6Sn_6$  ( $R = Tb, Dy, Ho, Er, Tm$ ) were synthesized via a self-flux method. Powder forms of rare-earth elements, abraded from metal blocks (99.99%), along with V

(powder, 99.9%) and Sn (shot, 99.999%) were loaded inside an alumina crucible with the molar ratio of 1:6:50 and then sealed in evacuated quartz tubes under  $10^{-4}$  torr pressure. The tubes were heated to 1125 °C and dwell for 24 hours before cooling down slowly at a rate of 2 °C/h. The single crystals were separated from the flux via centrifuging at 825 °C. Crystals grown via this method were generally a few millimeters (mm) in length and 1 mm in thickness [Fig. 1(c), inset]. The separated single crystals were subsequently cleaned with dilute HCl to remove the flux contamination.

Single-crystal XRD measurement on  $TmV_6Sn_6$  were carried out on a Bruker D8 Venture single-crystal diffractometer. XYZ centroids of 3012 reflections were collected and integrated using the Bruker SAINT software package. Powder XRD measurements on carefully grounded single-crystal samples were performed using a HUBER diffractometer at room temperature. Rietveld refinements were performed with the FULLPROF software package.

The magnetic properties, including DC susceptibility, and isothermal magnetization, were measured using a commercial magnetic properties measurement system (MPMS-III, Quantum Design) in the temperature range between 2 and 300 K under different external magnetic fields. Measurements from 0.4 to 1.8 K were performed using the same MPMS with the He3 option installed. Data measured using an empty holder

TABLE I. Fractional atomic coordinates and equivalent isotropic displacement parameters ( $\text{\AA}^2$ ) for  $\text{TmV}_6\text{Sn}_6$  from the refinement of single-crystal XRD data at  $T = 273$  K.  $U_{\text{eq}}$  is defined as  $1/3$  of the trace of the orthogonalized  $U_{ij}$  tensor.

Atom	Wyckoff pos.	$x$	$y$	$z$	$U_{\text{eq}}$
Tm	1a	0	0	0.5	0.053(3)
V	6i	0.5	0.5	0.748016(6)	0.0032(3)
Sn1	2e	0	0	0.83167(5)	0.050(3)
Sn2	2d	0.66667	0.33333	0.5	0.0029(3)
Sn3	2c	0.33333	0.66667	0	0.0037(3)

Reflections collected: 3012  
 $R_1: 2.54\%$ ;  $wR_2: 5.57\%$

was used as background to correct the diamagnetic signals in different sample environments at high and low temperatures. With the corrected data, a modified Curie-Weiss (CW) fit was performed from 150 to 300 K, i.e.,  $\chi(T) = \chi_0 + C/(T - \theta_{\text{CW}})$ , where  $\chi_0$  denotes the temperature-independent term arising from the Pauli and Van Vleck paramagnetism as well as diamagnetic signals of the nucleus, and  $\theta_{\text{CW}}$  is the CW temperature.

The resistivity and specific-heat data in the temperature range from 1.8 to 300 K were collected with a physical properties measurement system (Quantum Design). A specific-heat measurement on a nonmagnetic  $\text{YV}_6\text{Sn}_6$  single crystal was also measured and scaled to match that of  $\text{RV}_6\text{Sn}_6$  above 100 K, which is used as an estimate of lattice contribution  $C_{\text{lat}}$ . The magnetic heat capacity,  $C_{\text{mag}}(T)$ , was then obtained by subtracting the  $C_{\text{lat}}$  from the measured  $C_p(T)$ .

### III. CHARACTERIZATIONS

#### A. STRUCTURE

Powder XRD refinements confirm that all  $\text{RV}_6\text{Sn}_6$  compounds crystallize in the hexagonal  $\text{HfFe}_6\text{Ge}_6$ -type structure with space group  $P6/mmm$ . The crystallographic parameters of  $\text{TmV}_6\text{Sn}_6$  from single-crystal XRD are listed in Table I. As illustrated in Figs. 1(a) and 1(b), the ideal kagome layers

of V ions coordinated by Sn are separated by one  $R$ -triangle layer. With triangle layers of rare-earth elements and kagome layers of V elements stacked along the  $c$  axis, this series of compounds exhibits the same structure as  $\text{RMn}_6\text{Sn}_6$ . As expected, the cell parameters  $a$  and  $c$ , as well as the volume of unit cell increase monotonically with the increase of  $R^{3+}$  ionic radii [Figs. 1(d) and 1(e)]. These parameters are summarized in Table II.

#### B. MAGNETIC PROPERTIES

We use  $C_p(T)$ ,  $\chi(T)$ , and  $M(H)$  measurements to characterize the spin anisotropy of  $\text{RV}_6\text{Sn}_6$  and identify possible magnetic orderings. For each compound,  $\chi(T)$  and  $M(H)$  measurements were carried out under an external magnetic field applied both parallel and perpendicular to the  $c$  axis (Fig. 3). Modified CW fit to  $1/\chi(T)$  were performed at high (150–300 K) and low temperatures (6–10 K) to extract the effective moment  $\mu_{\text{eff}}$ , and CW temperature ( $\theta_{\text{CW}}$ ), respectively. As the magnetic moments of  $R$  ions tend to align at low temperatures, we extract low-temperature (6–10 K)  $\theta_{\text{CW}}$  to evaluate the magnetic interactions among them. Different temperature ranges of CW fitting contribute to the difference of the CW temperatures from [35]. In order to compare the magnetic properties of our samples with another study [35], CW fit at high temperatures (150–300 K) was also performed to extract high-temperature  $\theta_{\text{CW}}$ . Our results are basically consistent with those reported [35]. Some sample-dependent issues might still contribute to slight differences between the results in these two works. For all compounds and field applied in both directions, the numbers for  $\mu_{\text{eff}}$  are generally in agreement with the theoretical free-ion moment ( $\mu_{\text{theory}}$ ) expected for  $R^{3+}$  ions (Table II), consistent with the localized moment picture of  $R^{3+}$  magnetism.

#### I. $\text{TbV}_6\text{Sn}_6$

The  $C_{\text{mag}}$  of  $\text{TbV}_6\text{Sn}_6$  clearly shows a sharp peak at 4.4 K which can be seen clearly in  $C_{\text{mag}}$  [blue symbols in Fig. 2(b)]. A broad anomaly maximized around 40 K shows up in  $C_{\text{mag}}$  at high temperatures, which we attribute to the Schottky

TABLE II. Fitted parameters for  $\text{RV}_6\text{Sn}_6$  ( $R = \text{Tb} - \text{Tm}$ ), including (i) lattice parameters:  $a$ ,  $c$ ; (ii) magnetic property parameters: in-plane and out-of-plane CW temperature,  $\theta_{\text{CW}}^{ab}$ , and  $\theta_{\text{CW}}^c$ , in-plane and out-of-plane effective moment,  $\mu_{\text{eff}}^{ab}$  and  $\mu_{\text{eff}}^c$ .

	$\text{TbV}_6\text{Sn}_6$	$\text{DyV}_6\text{Sn}_6$	$\text{HoV}_6\text{Sn}_6$	$\text{ErV}_6\text{Sn}_6$	$\text{TmV}_6\text{Sn}_6$
Lattice parameters					
$a$ ( $\text{\AA}$ )	5.5200(2)	5.5162(2)	5.5126(5)	5.5084(3)	5.5043(3)
$c$ ( $\text{\AA}$ )	9.1830(6)	9.1792(5)	9.1756(9)	9.1736(6)	9.1714(6)
Magnetic property parameters					
Spin anisotropy	Easy axis (Ising)	Weak easy axis	Weak easy axis	Easy plane	Easy plane (XY)
$T_{N,c}$ (K)	4.4	3	2.5	–	–
Low temp. $\theta_{\text{CW}}^{ab}$ (K)	–	1.29	–10.73	0.07	–3.18
Low temp. $\theta_{\text{CW}}^c$ (K)	2.06	1.65	0.66	–	–
High temp. $\theta_{\text{CW}}^{ab}$ (K)	–50.47	–16.01	–14.42	4.42	12.69
High temp. $\theta_{\text{CW}}^c$ (K)	30.97	8.93	3.71	–33.46	–39.79
High temp. $\mu_{\text{eff}}^{ab}$ ( $\mu_B$ )	9.84	10.43	10.33	9.59	7.95
High temp. $\mu_{\text{eff}}^c$ ( $\mu_B$ )	9.47	10.88	10.29	9.75	7.49
$\mu_{\text{theory}}$ ( $\mu_B$ )	9.72	10.63	10.61	9.59	7.56

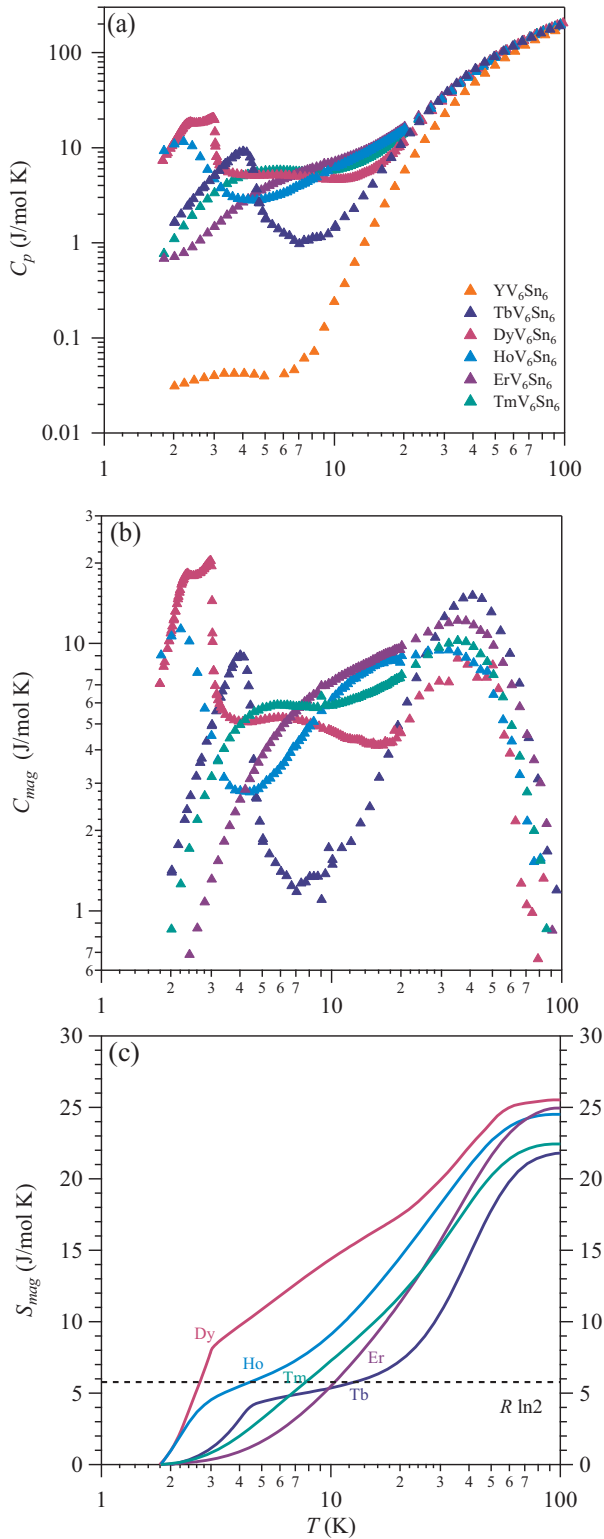


FIG. 2. (a) Measured  $C_p$  for  $RV_6Sn_6$  ( $R = Y, Tb - Tm$ ). (b) Magnetic heat capacity,  $C_{mag}$ , obtained by subtracting the lattice contribution from  $C_p$ . (c) Magnetic entropy obtained from integrating  $C_{mag}/T$  in (b).

anomaly of  $Tb^{3+}$  elevated crystal electric field. The integrated magnetic entropy  $S_{mag}$  reaches  $R \ln 2$  at 10 K, and is relatively flat until 20 K, indicating that the lowest crystal field level is

a non-Kramers doublet that is well separated from the higher levels. The fully recovered  $S_{mag}$  from 2 to 100 K reaches 21.77 J/mol K, which is close to the full single-ion magnetic entropy of  $R \ln 13$  expected for  $Tb^{3+}$  (total angular momentum  $J = 6$ ).

The  $\chi(T)$  of  $TbV_6Sn_6$  exhibits paramagnetic behavior at high temperatures, while at low temperatures, a broad anomaly in  $\chi_{ab}$  is observed around 60 K, which might be related to the broad  $C_{mag}$  anomaly around 50 K. A zero-field cooling and field-cooling divergence is observed below 4.4 K [Fig. 3(a) inset], consistent with the sharp peak seen in  $C_{mag}$ . It is noteworthy that the absolute value of  $\chi_c$  is two orders of magnitude larger than that of  $\chi_{ab}$ , indicating that the Tb magnetic moments tend to align along the crystallographic  $c$  axis. This is further confirmed by the  $M(H)$  at 0.4 K [Fig. 3(f)], where the magnetization along the  $c$  axis rapidly increases and saturates above 0.5 T to a moment of  $9.72\mu_B/Tb$  while the number is merely  $1.25\mu_B/Tb$  when the field is applied within the  $ab$  plane. With strong easy-axis anisotropy, a modified CW fit of  $\chi_c$  at low temperatures yields  $\theta_{CW} = 2.06$  K, suggesting an overall weak ferromagnetic interaction.

## 2. $DyV_6Sn_6$ and $HoV_6Sn_6$

Similar to that of  $TbV_6Sn_6$ , we can identify a clear signature of magnetic ordering in  $DyV_6Sn_6$  and  $HoV_6Sn_6$  from  $C_{mag}$ , at 2.4 and 2.5 K, respectively. Interestingly, for  $DyV_6Sn_6$ , an additional transition at 3 K is present in  $C_{mag}$  whose origin is subject to further investigations. Broad anomalies between 20 and 50 K also show up in  $C_{mag}$  at high temperatures due to the Schottky anomaly of crystal field effects. For both samples, the integrated magnetic entropy  $S_{mag}$  continuously increases above the magnetic ordering temperature, whose values quickly exceed  $R \ln 2$ . This observation clearly demonstrates the existence of low-lying crystal field, meaning that the low-temperature rare-earth magnetism cannot be treated as effective spin 1/2. The fully recovered  $S_{mag}$  from 2 to 100 K reaches 25.52 J/mol K for  $DyV_6Sn_6$  and 24.51 J/mol K for  $HoV_6Sn_6$ , which are in reasonable agreement with the full single-ion magnetic entropy of  $R \ln 15$  and  $R \ln 16$  expected for  $Dy^{3+}$  ( $J = 15/2$ ) and  $Ho^{3+}$  ( $J = 8$ ), respectively.

For  $DyV_6Sn_6$ , an abrupt anomaly in  $\chi_c$  was observed at around 3 K while  $\chi_{ab}$  becomes flat below 2.4 K, consistent with the two sharp peaks seen in  $C_{mag}$ . For  $HoV_6Sn_6$ ,  $\chi_c$  becomes flat around 2.5 K while a broad peak is observed in  $\chi_{ab}$  at this temperature, consistent with the sharp peak seen in  $C_{mag}$ . It is noteworthy that the absolute value of  $\chi_c$  and  $\chi_{ab}$  are in the same order of magnitude for  $DyV_6Sn_6$  and  $HoV_6Sn_6$ , indicating that the Dy and Ho magnetic moments tend to exhibit Heisenberg-like behavior. This is further confirmed by the  $M(H)$  at 0.4 K [Figs. 3(f) and 3(h)]. For  $DyV_6Sn_6$ , the magnetization along the  $c$  axis rapidly increases above 0.5 T and stays flat until 6 T where a jump to another plateau of  $9.52\mu_B/Dy$  appears [Fig. 4(g) inset]. Accordingly, the  $M_{ab}$  reaches  $6.73\mu_B/Dy$  at 7 T. For  $HoV_6Sn_6$ , the magnetization along the  $c$  axis rapidly saturates above 0.3 T to a moment of  $8.81\mu_B/Ho$  while the moment keeps increasing to  $9.71\mu_B/Ho$  until 7 T when the field is applied with the  $ab$  plane. This indicates the single-ion magnetism is still anisotropic and weak easy axis. The low-temperature CW fit of  $DyV_6Sn_6$

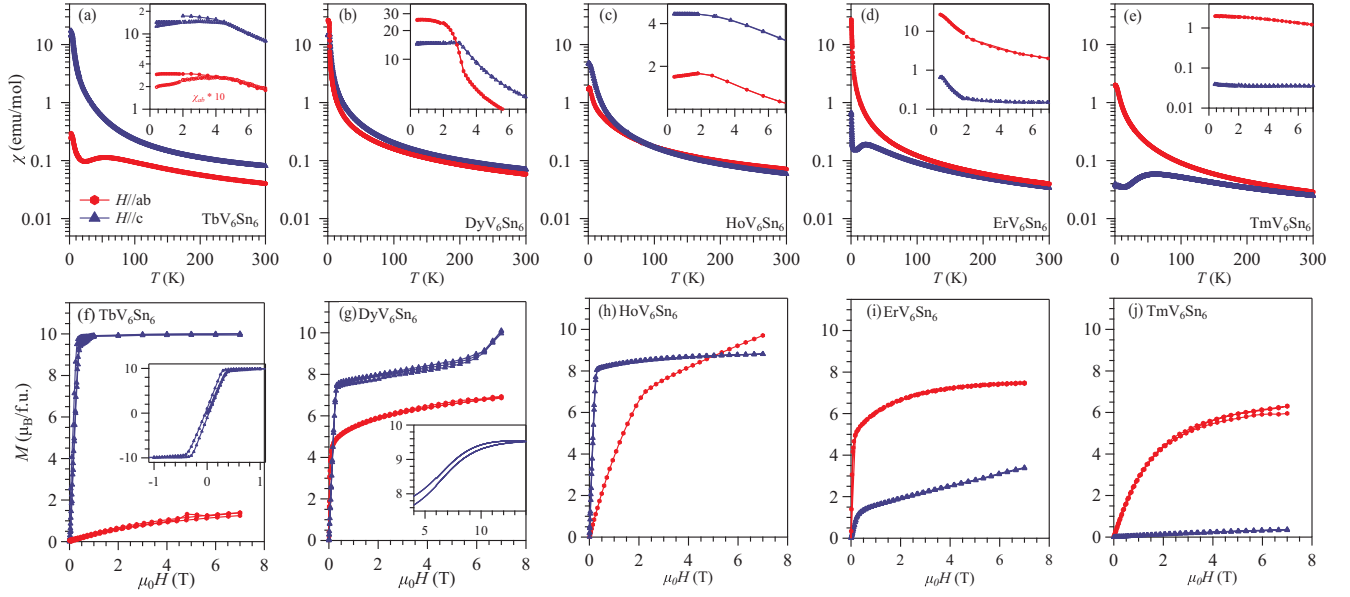


FIG. 3. (a)–(e) Magnetic susceptibility of  $RV_6Sn_6$  ( $R = Tb - Tm$ ) in a log-linear scale. An external magnetic field of 0.1 T was applied both parallel (blue triangle) and perpendicular (red circle) to the  $c$  axis. Insets: zoom-in data at low temperatures from 0.4 to 7 K. (f)–(j) Field dependence of isothermal magnetization measured at 0.4 K, with field applied parallel (blue triangle) and perpendicular (red circle) to the  $c$  axis. Insets:  $M(H)$  curves in extended regions when hysteresis loop is present.

gives  $\theta_{CW} = 1.29$  and  $1.65$  K for  $\chi_{ab}$  and  $\chi_c$ , respectively, suggesting an overall weak ferromagnetic interaction for both directions. Accordingly, the same CW fit to  $HoV_6Sn_6$  yields  $\theta_{CW}^{ab} = -10.73$  K and  $\theta_{CW}^c = -0.66$  K, indicating the dominating magnetic interaction is antiferromagnetic between  $Ho^{3+}$  moments in the  $ab$  plane.

### 3. $ErV_6Sn_6$ and $TmV_6Sn_6$

Different from the three compounds discussed above, we found no sign of magnetic ordering down to 1.8 K in  $ErV_6Sn_6$  or  $TmV_6Sn_6$  from  $C_{mag}$ . Instead,  $C_{mag}$  of  $TmV_6Sn_6$  shows a broad peak below 10 K, likely due to the development of short-ranged magnetic correlations, which is, however, absent in  $ErV_6Sn_6$ . The integrated magnetic entropy  $S_{mag}$  keeps increasing with neither anomaly nor plateaus observed until 60 K, suggesting the energy scale of the crystal fields are in the order of several meV. For  $ErV_6Sn_6$  and  $TmV_6Sn_6$ , the fully recovered  $S_{mag}$  from 2 to 100 K reaches 24.95 and 22.43 J/mol K, respectively, which is close to the full single-ion magnetic entropy of  $R \ln 16$  and  $R \ln 13$  expected for  $Er^{3+}$  ( $J = 15/2$ ) and  $Tm^{3+}$  ( $J = 6$ ).

For  $ErV_6Sn_6$  and  $TmV_6Sn_6$ , there is no anomaly observed in  $\chi_{ab}$ , confirming the absence of magnetic ordering down to 0.4 K. Broad anomalies in  $\chi_c$  are observed around 20 and 60 K, which might be related to crystal field effects. No anomaly is observed in  $\chi_{ab}$  and  $\chi_c$  of  $ErV_6Sn_6$  and  $TmV_6Sn_6$  at low temperatures, consistent with the hump in  $C_{mag}$ . It is noteworthy that the absolute value of  $\chi_{ab}$  is two orders of magnitude larger than that of  $\chi_c$  for these two compounds, indicating that the Er and Tm magnetic moments tend to align in the  $ab$  plane. This is further confirmed by the  $M(H)$  at 0.4 K [Fig. 3(f)]. For  $ErV_6Sn_6$ , the magnetization in the  $ab$  plane rapidly increases and saturates above 0.5 T to a moment of

$7.41 \mu_B/Er$  while the moment keeps increasing to  $3.39 \mu_B/Er$  at 7 T after a transition appeared at around 0.4 T when the field is applied along the  $c$  axis. For  $TmV_6Sn_6$ , the magnetization in the  $ab$  plane rapidly reaches  $6.29 \mu_B/Tm$  at 7 T, in sharp contrast to a number of  $0.36 \mu_B/Er$  when the field is applied along the  $c$  axis, suggesting that the  $TmV_6Sn_6$  can be properly described by an  $XY$  effective spin model. With easy-plane anisotropy for both compounds, a low-temperature CW fit of  $\chi_{ab}$  gives  $\theta_{CW}^{ab} = 0.07$  K for  $ErV_6Sn_6$  and  $\theta_{CW}^{ab} = -3.18$  K for  $TmV_6Sn_6$ . This seems to suggest the average in-plane spin-spin interaction is antiferromagnetic for  $TmV_6Sn_6$  while the magnitude is negligible in  $ErV_6Sn_6$ .

### C. Transport properties

The main panel of Fig. 4(a) shows the temperature dependence of resistivity  $\rho(T)$  at zero field for  $RV_6Sn_6$  ( $R = Tb - Tm$ ) compounds, and the typical metallic behavior can be seen for all samples. At low temperatures, an anomaly exhibits in the resistivity, which is associated with the formation of the magnetic order of  $Tb^{3+}$ ,  $Dy^{3+}$ , and  $Ho^{3+}$  ions. The inset of Fig. 4(a) shows the enlarged view of resistivity in the low-temperature range; the sharp drop in resistivity at the magnetic ordering temperatures can be seen more clearly. For  $ErV_6Sn_6$  and  $TmV_6Sn_6$ , an anomaly was also observed at low temperatures even without magnetic order. When we increase the magnetic field to 1 T, the anomaly was suppressed in resistivity. We thus attribute this consistent drop in  $\rho(T)$  to the scattering of the conduction electrons by optical phonons if the magnetic  $s-f$  contribution is neglected [36]. The possibility of Sn impurity superconductivity cannot be ruled out either. Here, we vertically shift all the resistivity curves for clarity.

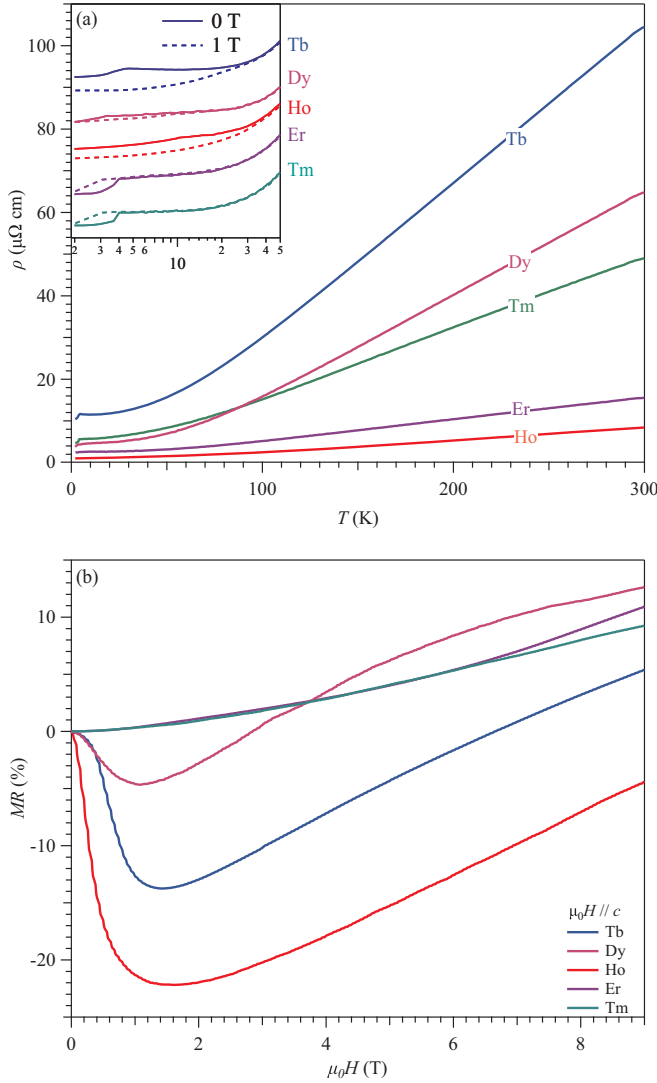


FIG. 4. (a) The temperature dependence of normalized resistivity  $\rho/\rho(300\text{ K})$  of  $RV_6\text{Sn}_6$  ( $R = \text{Tb} - \text{Tm}$ ). Inset: temperature dependence of resistivity measured without and with magnetic field of 1 T along the  $c$  axis. (b) The magnetic field dependence of magnetoresistivity of  $RV_6\text{Sn}_6$  with an external magnetic field applied along the  $c$  axis.

Moreover, the transport behavior has strong dependence on the  $R$  ions, which we can see more clearly in the magnetoresistance (MR) at 2 K. As shown in Fig. 4(b),  $\text{ErV}_6\text{Sn}_6$  and  $\text{TmV}_6\text{Sn}_6$  exhibit a positive MR, while for  $R = \text{Tb}, \text{Dy}$ , and  $\text{Ho}$ , they show negative MR behavior. Since the localized  $R^{3+}$  ions do not participate directly in the electrical conduction, the observed distinct magnetoresistance behaviors in Fig. 4(b) can be ascribed in a conventional scenario to the different scattering processes of conduction electrons by the  $R^{3+}$  ions possessing different magnetic ground states and single-ion anisotropy. Consistent with the isothermal magnetization data shown in Fig. 3, the easy alignment of  $R^{3+}$  moments for  $R = \text{Tb}, \text{Dy}$ , and  $\text{Ho}$  along the  $c$  axis at low fields would reduce the scattering of conduction electrons and give rise to a negative magnetoresistance. Once the  $R^{3+}$  moments are aligned at low fields, the negative magnetoresistance is reverted to posi-

tive one at higher fields as shown in Fig. 4(b). In contrast, the  $c$  axis field can barely influence the  $R^{3+}$  moments with strong easy-plane anisotropy for  $R = \text{Er}$  and  $\text{Tm}$ , which thus display typical positive magnetoresistance behaviors due to the effect of Lorentz force. On the other hand, further investigations are needed to figure out whether the observed distinct phenomenon is associated with some nontrivial mechanisms; for example, the band topology of the vanadium kagome layers might be tuned by the magnetic ordering and/or the single-ion anisotropy of  $R^{3+}$  ions.

To further gain insights into the carrier information including carriers concentration and mobility of the series of  $RV_6\text{Sn}_6$  samples, Hall resistivity measurements were performed. As displayed in Figs. 5(a)–5(e), the Hall resistivity  $\rho_{xy}(H)$  was measured at various temperatures for the whole series of  $RV_6\text{Sn}_6$  samples. The current was applied within the  $ab$  plane and the magnetic field applied along the  $c$  axis. The  $\rho_{xy}(H)$  ( $\rho_{xx}$ ) data were antisymmetrized (symmetrized) with respect to the data collected between  $+9$  and  $-9$  T. As can be seen, the  $\rho_{xy}(H)$  for these compounds share similar behaviors with increasing temperature gradually. Specifically, the  $\rho_{xy}(H)$  curves are linear with a hole-dominated band feature at temperatures above 200 K and the nonlinear behavior emerges at low temperatures, in agreement with the multiband character. To obtain the carrier concentration and mobility in these compounds, a two-band model was employed to fit the Hall conductivity  $\sigma_{xy}(H)$  at different temperatures. Here, the longitudinal resistivity  $\rho_{xx}$  curves were also measured at the same time. The Hall conductivity  $\sigma_{xy}(H)$  and two-carrier model were calculated based on the equation

$$\sigma_{xy} = -\frac{\rho_{xy}}{\rho_{xy}^2 + \rho_{xx}^2}, \quad (1)$$

$$\sigma_{xy} = \left[ n_h \mu_h^2 \frac{1}{1 + (\mu_h B)^2} - n_e \mu_e^2 \frac{1}{1 + (\mu_e B)^2} \right] eB, \quad (2)$$

where  $n_e$  and  $n_h$  are the carrier density of electrons and holes, while  $\mu_e$  and  $\mu_h$  are the mobility of electrons and holes.

Figures 5(f)–5(j) show the fitting results of carrier density and mobility. Above 150 K, the density of the hole for each sample is higher than that of the electron. The hole mobility of  $\text{TbV}_6\text{Sn}_6$ ,  $\text{DyV}_6\text{Sn}_6$ , and  $\text{TmV}_6\text{Sn}_6$  is also dominant while electron and hole mobilities possess similar values for  $\text{HoV}_6\text{Sn}_6$  and  $\text{ErV}_6\text{Sn}_6$  above 150 K. It is also verified that  $\rho_{xy}$  of all these samples exhibits hole-dominated behaviors. At temperatures below 100 K, a divergence for carrier density appears and seems to become stronger upon cooling down continuously. For  $\text{DyV}_6\text{Sn}_6$ ,  $\text{ErV}_6\text{Sn}_6$ , and  $\text{TmV}_6\text{Sn}_6$ , the mobility of electrons and holes becomes comparable below 100 K. For  $\text{TbV}_6\text{Sn}_6$ , the electron carriers with larger mobility become dominant over the hole carriers while the carrier mobility of  $\text{HoV}_6\text{Sn}_6$  has the opposite trend. In general, all samples exhibit hole-dominated behavior at high temperatures while two-band behavior prevails below 100 K, consistent with the  $\rho_{xy}$  data shown in Figs. 5(a)–5(e).

#### IV. DISCUSSION AND SUMMARY

In this study, we synthesized a series of  $\text{HfFe}_6\text{Ge}_6$ -type kagome metals  $RV_6\text{Sn}_6$  ( $R = \text{Tb} - \text{Tm}$ ) single crystals

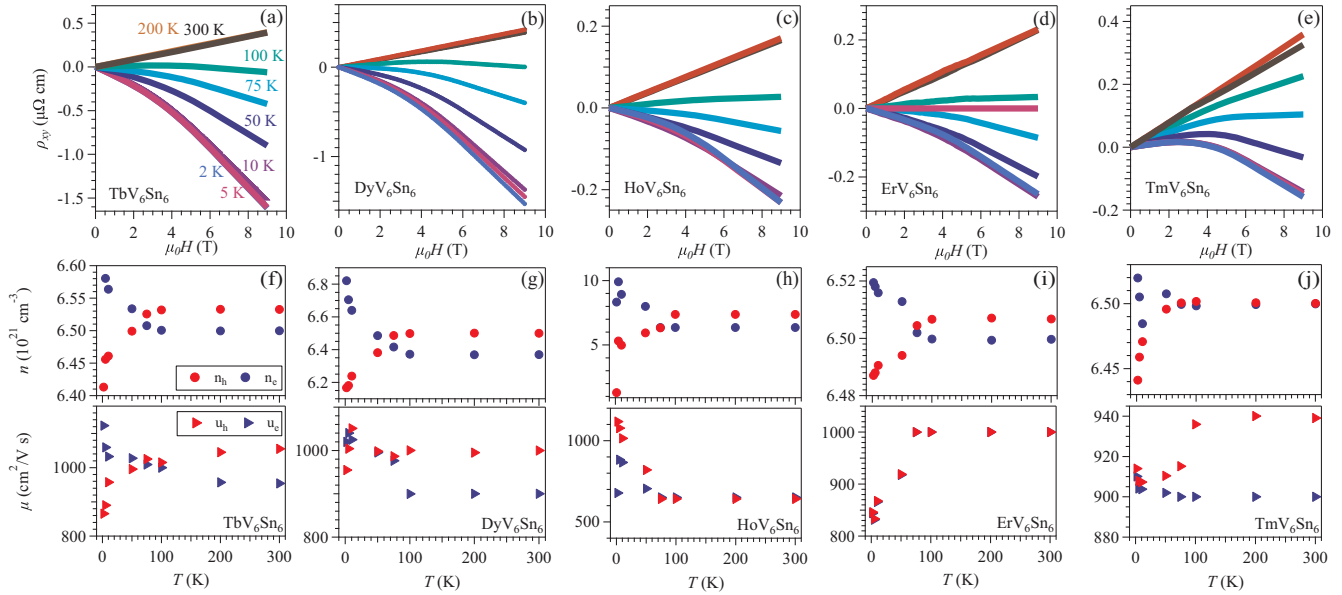


FIG. 5. (a)–(e) Magnetic field dependence of longitudinal resistivity  $\rho_{xy}$  measured at different temperatures. (f)–(j) Temperature dependence of carrier density,  $n$ , and mobility,  $\mu$ , obtained from Hall conductivity fit.

and characterized their physical properties. Compared to the kagome superconductors  $AV_3Sb_5$  ( $A = K, Rb, Cs$ ), no CDW or superconductivity was observed down to 0.4 K in  $RV_6Sn_6$  ( $R = Tb - Tm$ ).

In comparison with  $RMn_6Sn_6$ , these V-based kagome metals have similar evolution of spin anisotropy for the rare-earth elements as their Mn-based counterparts [27]. Specifically,  $TbV_6Sn_6$  exhibits strong Ising anisotropy, for which the magnetic moments tend to align to the  $c$  axis while  $TmV_6Sn_6$  and  $ErV_6Sn_6$  possess easy-plane anisotropy with moments lying in the  $ab$  plane at low temperatures. For  $R = Ho, Dy$ , more isotropic behaviors are observed. The dramatically different spin anisotropies originate from different crystal-field schemes of  $R^{3+}$  ions, whose effects further mediate the exchange couplings between  $4f$  and  $3d$  electrons, and thus becomes the key to engineer the magnetic structure and topological properties of  $RMn_6Sn_6$  [16,27,28]. Moreover, the  $XY$  anisotropy of  $Tm^{3+}$  in  $TmMn_6Sn_6$  is very surprising since all non-Kramers doublets should be described by an Ising moment of effective spin-1/2 [37], like that found in  $TbMn_6Sn_6$ . This means the magnetism of  $TmMn_6Sn_6$  must involve more than one crystal-field level and request a different theoretical treatment. The absence of magnetic order in  $TmV_6Sn_6$  in contrast to a moderate spin-spin coupling ( $\theta_{CW}^{ab} = -3.18$  K) may be due to the thermal fluctuations according to

the Mermin-Wagner theorem [38]. Consider the complexity of long-ranged Ruderman-Kittel-Kasuya-Yosida interactions, it calls for further investigations to understand the absence of magnetic order in  $TmV_6Sn_6$ .

It has been reported that  $YV_6Sn_6$  and  $GdV_6Sn_6$  show qualitatively similar band structures in the paramagnetic state [33]. As predicted by the density functional theory, the density of states in these materials are dominated by V  $d$  states. Thus our new synthesized materials,  $RV_6Sn_6$  ( $R = Tb - Tm$ ), are expected to possess a similar electronic band structure.

#### ACKNOWLEDGMENTS

This work is supported by the National Key R&D Program of China (Grants No. 2018YFA0305700 and No. 2021YFA1400200), the National Natural Science Foundation of China (Grants No. 12025408, No. 11874400, No. 11834016, No. 11921004, and No. 12174424), Beijing Natural Science Foundation (Grant No. Z190008), the Strategic Priority Research Program and Key Research Program of Frontier Sciences of CAS (Grants No. XDB25000000, No. XDB33000000, and No. QYZDB-SSW-SLH013), the CAS Interdisciplinary Innovation Team (Grant No. JCTD-2019-01), and Lujiaxi international group funding of K. C. Wong Education Foundation (Grant No. GJTD-2020-01).

- [1] Y. Zhou, K. Kanoda, and T.-K. Ng, Quantum spin liquid states, *Rev. Mod. Phys.* **89**, 025003 (2017).
- [2] B. Keimer and J. Moore, The physics of quantum materials, *Nat. Phys.* **13**, 1045 (2017).
- [3] T. Park, M. Ye, and L. Balents, Electronic instabilities of kagome metals: Saddle points and Landau theory, *Phys. Rev. B* **104**, 035142 (2021).
- [4] J.-X. Yin, S. S. Zhang, H. Li, K. Jiang, G. Chang, B. Zhang, B. Lian, C. Xiang, I. Belopolski, H. Zheng *et al.*,

Giant and anisotropic many-body spin-orbit tunability in a strongly correlated kagome magnet, *Nature (London)* **562**, 91 (2018).

- [5] G. Xu, B. Lian, and S.-C. Zhang, Intrinsic Quantum Anomalous Hall Effect in the Kagome Lattice  $Cs_2LiMn_3F_{12}$ , *Phys. Rev. Lett.* **115**, 186802 (2015).
- [6] M. Pereiro, D. Yudin, J. Chico, C. Etz, O. Eriksson, and A. Bergman, Topological excitations in a kagome magnet, *Nat. Commun.* **5**, 4815 (2014).

- [7] H. Li, B. Ding, J. Chen, Z. Li, Z. Hou, E. Liu, H. Zhang, X. Xi, G. Wu, and W. Wang, Large topological Hall effect in a geometrically frustrated kagome magnet  $\text{Fe}_3\text{Sn}_2$ , *Appl. Phys. Lett.* **114**, 192408 (2019).
- [8] Z. Y. Liu, T. Zhang, S. X. Xu, P. T. Yang, Q. Wang, H. C. Lei, Y. Sui, Y. Uwatoko, B. S. Wang, H. M. Weng *et al.*, Pressure effect on the anomalous Hall effect of ferromagnetic Weyl semimetal  $\text{Co}_3\text{Sn}_2\text{S}_2$ , *Phys. Rev. Mater.* **4**, 044203 (2020).
- [9] M. R. Norman, Colloquium: Herbertsmithite and the search for the quantum spin liquid, *Rev. Mod. Phys.* **88**, 041002 (2016).
- [10] M. J. Lawler, A. Paramekanti, Y. B. Kim, and L. Balents, Gapless Spin Liquids on the Three-Dimensional Hyperkagome Lattice of  $\text{Na}_4\text{Ir}_3\text{O}_8$ , *Phys. Rev. Lett.* **101**, 197202 (2008).
- [11] N. J. Ghimire and I. I. Mazin, Topology and correlations on the kagome lattice, *Nat. Mater.* **19**, 137 (2020).
- [12] Z. Li, J. Zhuang, L. Wang, H. Feng, Q. Gao, X. Xu, W. Hao, X. Wang, C. Zhang, K. Wu *et al.*, Realization of flat band with possible nontrivial topology in electronic kagome lattice, *Sci. Adv.* **4**, eaau4511 (2018).
- [13] L. Ye, M. Kang, J. Liu, F. Von Cube, C. R. Wicker, T. Suzuki, C. Jozwiak, A. Bostwick, E. Rotenberg, D. C. Bell *et al.*, Massive Dirac fermions in a ferromagnetic kagome metal, *Nature (London)* **555**, 638 (2018).
- [14] X. Zhang, L. Jin, X. Dai, and G. Liu, Topological type-II nodal line semimetal and Dirac semimetal state in stable kagome compound  $\text{Mg}_3\text{Bi}_2$ , *J. Phys. Chem. Lett.* **8**, 4814 (2017).
- [15] M. Li, Q. Wang, G. Wang, Z. Yuan, W. Song, R. Lou, Z. Liu, Y. Huang, Z. Liu, H. Lei *et al.*, Dirac cone, flat band and saddle point in kagome magnet  $\text{YMn}_6\text{Sn}_6$ , *Nat. Commun.* **12**, 3129 (2021).
- [16] J.-X. Yin, W. Ma, T. A. Cochran, X. Xu, S. S. Zhang, H.-J. Tien, N. Shumiya, G. Cheng, K. Jiang, B. Lian *et al.*, Quantum-limit Chern topological magnetism in  $\text{TbMn}_6\text{Sn}_6$ , *Nature (London)* **583**, 533 (2020).
- [17] B. R. Ortiz, L. C. Gomes, J. R. Morey, M. Winiarski, M. Bordelon, J. S. Mangum, I. W. H. Oswald, J. A. Rodriguez-Rivera, J. R. Neilson, S. D. Wilson *et al.*, New kagome prototype materials: Discovery of  $\text{KV}_3\text{Sb}_5$ ,  $\text{RbV}_3\text{Sb}_5$ , and  $\text{CsV}_3\text{Sb}_5$ , *Phys. Rev. Mater.* **3**, 094407 (2019).
- [18] B. R. Ortiz, P. M. Sarte, E. M. Kenney, M. J. Graf, S. M. L. Teicher, R. Seshadri, and S. D. Wilson, Superconductivity in the  $Z_2$  kagome metal  $\text{KV}_3\text{Sb}_5$ , *Phys. Rev. Mater.* **5**, 034801 (2021).
- [19] Q. Yin, Z. Tu, C. Gong, Y. Fu, S. Yan, and H. Lei, Superconductivity and normal-state properties of kagome metal  $\text{RbV}_3\text{Sb}_5$  single crystals, *Chin. Phys. Lett.* **38**, 037403 (2021).
- [20] B. R. Ortiz, S. M. L. Teicher, Y. Hu, J. L. Zuo, P. M. Sarte, E. C. Schueller, A. M. Milinda Abeykoon, M. J. Krogstad, S. Rosenkranz, R. Osborn *et al.*,  $\text{CsV}_3\text{Sb}_5$ : A  $Z_2$  Topological Kagome Metal with a Superconducting Ground State, *Phys. Rev. Lett.* **125**, 247002 (2020).
- [21] Y.-X. Jiang, J.-X. Yin, M. M. Denner, N. Shumiya, B. R. Ortiz, G. Xu, Z. Guguchia, J. He, M. S. Hossain, X. Liu *et al.*, Unconventional chiral charge order in kagome superconductor  $\text{KV}_3\text{Sb}_5$ , *Nat. Mater.* **20**, 1353 (2021).
- [22] S. Ni, S. Ma, Y. Zhang, J. Yuan, H. Yang, Z. Lu, N. Wang, J. Sun, Z. Zhao, D. Li *et al.*, Anisotropic superconducting properties of kagome metal  $\text{CsV}_3\text{Sb}_5$ , *Chin. Phys. Lett.* **38**, 057403 (2021).
- [23] C. Mu, Q. Yin, Z. Tu, C. Gong, H. Lei, Z. Li, and J. Luo, S-wave superconductivity in kagome metal  $\text{CsV}_3\text{Sb}_5$  revealed by  $^{121/123}\text{Sb}$  NQR and 51V NMR measurements, *Chin. Phys. Lett.* **38**, 077402 (2021).
- [24] K. Y. Chen, N. N. Wang, Q. W. Yin, Y. H. Gu, K. Jiang, Z. J. Tu, C. S. Gong, Y. Uwatoko, J. P. Sun, H. C. Lei *et al.*, Double Superconducting Dome and Triple Enhancement of  $T_c$  in the Kagome Superconductor  $\text{CsV}_3\text{Sb}_5$  under High Pressure, *Phys. Rev. Lett.* **126**, 247001 (2021).
- [25] F. H. Yu, D. H. Ma, W. Z. Zhuo, S. Q. Liu, X. K. Wen, B. Lei, J. J. Ying, and X. H. Chen, Unusual competition of superconductivity and charge-density-wave state in a compressed topological kagome metal, *Nat. Commun.* **12**, 3645 (2021).
- [26] X. Chen, X. Zhan, X. Wang, J. Deng, X.-B. Liu, X. Chen, J.-G. Guo, and X. Chen, Highly robust reentrant superconductivity in  $\text{CsV}_3\text{Sb}_5$  under pressure, *Chin. Phys. Lett.* **38**, 057402 (2021).
- [27] W. Ma, X. Xu, J.-X. Yin, H. Yang, H. Zhou, Z.-J. Cheng, Y. Huang, Z. Qu, F. Wang, M. Z. Hasan *et al.*, Rare Earth Engineering in  $\text{RMn}_6\text{Sn}_6$  ( $R = \text{Gd} - \text{Tm}, \text{Lu}$ ) Topological Kagome Magnets, *Phys. Rev. Lett.* **126**, 246602 (2021).
- [28] L. Gao, S. Shen, Q. Wang, W. Shi, Y. Zhao, C. Li, W. Cao, C. Pei, J.-Y. Ge, G. Li *et al.*, Anomalous Hall effect in ferrimagnetic metal  $\text{RMn}_6\text{Sn}_6$  ( $R = \text{Tb}, \text{Dy}, \text{Ho}$ ) with clean Mn kagome lattice, *Appl. Phys. Lett.* **119**, 092405 (2021).
- [29] G. Venturini, B. C. El Idrissi, and B. Malaman, Magnetic properties of  $\text{RMn}_6\text{Sn}_6$  ( $R = \text{Sc}, \text{Y}, \text{Gd} - \text{Tm}, \text{Lu}$ ) compounds with  $\text{HfFe}_6\text{Ge}_6$  type structure, *J. Magn. Magn. Mater.* **94**, 35 (1991).
- [30] B. Malaman, G. Venturini, R. Welter, J. Sanchez, P. Vulliet, and E. Ressouche, Magnetic properties of  $\text{RMn}_6\text{Sn}_6$  ( $R = \text{Gd} - \text{Er}$ ) compounds from neutron diffraction and Mössbauer measurements, *J. Magn. Magn. Mater.* **202**, 519 (1999).
- [31] D. M. Clatterback and K. A. Gschneidner, Jr., Magnetic properties of  $\text{RMn}_6\text{Sn}_6$  ( $R = \text{Tb}, \text{Ho}, \text{Er}, \text{Tm}, \text{Lu}$ ) single crystals, *J. Magn. Magn. Mater.* **207**, 78 (1999).
- [32] S. Peng, Y. Han, G. Pokharel, J. Shen, Z. Li, M. Hashimoto, D. Lu, B. R. Ortiz, Y. Luo, H. Li *et al.*, Realizing Kagome Band Structure in Two-Dimensional Kagome Surface States of  $\text{RV}_6\text{Sn}_6$  ( $R = \text{Gd}, \text{Ho}$ ), *Phys. Rev. Lett.* **127**, 266401 (2021).
- [33] G. Pokharel, S. M. L. Teicher, B. R. Ortiz, P. M. Sarte, G. Wu, S. Peng, J. He, R. Seshadri, and S. D. Wilson, Electronic properties of the topological kagome metals  $\text{YV}_6\text{Sn}_6$  and  $\text{GdV}_6\text{Sn}_6$ , *Phys. Rev. B* **104**, 235139 (2021).
- [34] H. W. S. Arachchige, W. R. Meier, M. Marshall, T. Matsuoka, R. Xue, M. A. McGuire, R. P. Hermann, H. Cao, and D. Mandrus, Charge density wave in kagome lattice intermetallic  $\text{ScV}_6\text{Sn}_6$ , *arXiv:2205.04582*.
- [35] E. M. Jeonghun Lee, Anisotropic magnetic property of single crystals  $\text{RV}_6\text{Sn}_6$  ( $R = \text{Y}, \text{Gd} - \text{Tm}, \text{Lu}$ ), *arXiv:2206.02924*.
- [36] K. Durczewski, Z. Gajek, and J. Mucha, Influence of electron-phonon interaction and crystal field on thermal and electrical resistivity in rare earth intermetallics, *Eur. Phys. J. B* **93**, 95 (2020).
- [37] Z. Dun, X. Bai, M. B. Stone, H. Zhou, and M. Mourigal, Effective point-charge analysis of crystal fields: Application to rare-earth pyrochlores and tripod kagome magnets  $\text{R}_3\text{Mg}_2\text{Sb}_3\text{O}_{14}$ , *Phys. Rev. Res.* **3**, 023012 (2021).
- [38] N. D. Mermin and H. Wagner, Absence of Ferromagnetism or Antiferromagnetism in One- or Two-Dimensional Isotropic Heisenberg Models, *Phys. Rev. Lett.* **17**, 1133 (1966).